

On Von Kármán Vortex Street Behind a 2D Circular Cylinder

Kamil Dylewicz

1 Introduction

The von Kármán vortex street is a well-known phenomenon in fluid mechanics and occurs behind bluff bodies, above some critical Reynolds number, as a result of boundary layer separation. The separated boundary layers form two shear layers that induce various instabilities, which eventually give rise to the von Kármán vortex shedding (Ausoni et al. 2006, Mittal et al. 2008). The bluff body wakes are of great engineering interest as they can generate noise or induce structural vibrations and, given agreement between natural frequency of the structure and the frequency of the vortex shedding, cause catastrophic failures (Williamson 1996). An example of such failure is the infamous collapse of the Tacoma Narrows Bridge (Larsen 2000).

This work presents results of direct numerical simulation (DNS) of flow past a 2D circular cylinder with particular attention paid to the von Kármán vortex street generated and its influence on the cylinder itself. An attempt is made to quantify the size of the separation bubble behind the cylinder for a laminar steady flow regime which is defined, by Williamson (1996), as the flow below Reynolds number, $Re (= Ud/\nu)$, of 49.

As the Reynolds number increases the influence of viscosity on the wake decreases leading to Reynolds stresses becoming dominant over the viscous ones. Roshko (1993) suggests that the unsteadiness and wake instability downstream of the cylinder start at Reynolds number about 50. A more detailed flow regimes breakdown is presented by Williamson (1996), who defines a stable laminar vortex shedding regime for $50 \leq Re \leq 150$, a transitional regime for $150 \leq Re \leq 300$ and an irregular regime for $300 \leq Re \leq 10E4$ where the velocity variations are characterised by noticeable irregularities. Another objective of this work is to determine the Strouhal number, $St (= fd/U)$, of the vortex shedding for Reynolds numbers in range $80 \leq Re \leq 10E4$.

Over the past decades, many attempts have been made to quantify and analyse the drag coefficient of bluff bodies. A detailed overview of this topic is presented by Roshko (1993). This study aims to show the relation between drag coefficient, C_D , and Reynolds number for a circular 2D cylinder.

2 Numerical approach

To create a geometry and then perform the DNS, two pieces of open source software were used that are called Gmsh and openFOAM respectively. The former is a 3D finite element grid generator with a CAD engine and post-processing capabilities (Geuzaine & Remacle 2009). The openFOAM is a CFD toolbox (OpenCFD 2019) that provides a range of solvers, where each has its specific purpose. This work implements the solver called icoFoam that is used to analyse incompressible and transient flows (OpenCFD 2018).

2.1 Governing equations

As this work uses direct numerical simulations of the incompressible flow, the governing equations are the incompressible, unsteady Navier-Stokes (NS) equations, which have the following form

$$\nabla \cdot \mathbf{u} = 0 \tag{1a}$$

$$\frac{\partial}{\partial t} \mathbf{u} + \nabla \cdot (\mathbf{u} \otimes \mathbf{u}) - \nabla \cdot (\nu \nabla \mathbf{u}) = -\nabla p \tag{1b}$$

where t is time, \mathbf{u} is a velocity vector, ν is a kinematic viscosity and p is a kinematic pressure. Importantly, the above equations are in the dimensional form and that's how they are solved by openFOAM. Therefore, the Reynolds number, that is of great importance for this analysis, will be manipulated by adjusting the kinematic viscosity accordingly. The NS equations are solved using Pressure Implicit with Splitting of Operations (PISO) algorithm proposed by Issa (1986), which is incorporated in the source code of icoFoam. The temporal integration scheme used was the Euler implicit time scheme that is a first order, implicit integration scheme. The gradient and divergence schemes used were Gaussian ones with linear interpolations (OpenCFD 2018).

2.2 Computational setup

The computational domain has been created using an open source software Gmsh v4.71 and stretches from $(-5.0 -5.0 0.0)$ to $(25.0 5.0 1.0)$, where the unit associated with the geometry is a meter. The cylinder diameter (d), which happens to be also the characteristics length in Reynolds and Strouhal numbers definitions, is equal to 1 unit. Based on this length, the rest of the geometry is scaled as shown in figure 1. In order to monitor convergence of the simulation two probes have been placed withing the flow field and their schematic positions are shown in the same figure. The exact coordinates are $(1.0 0.0 0.0)$ and $(10 2.5 0.0)$ for probes 1 and 2 respectively.

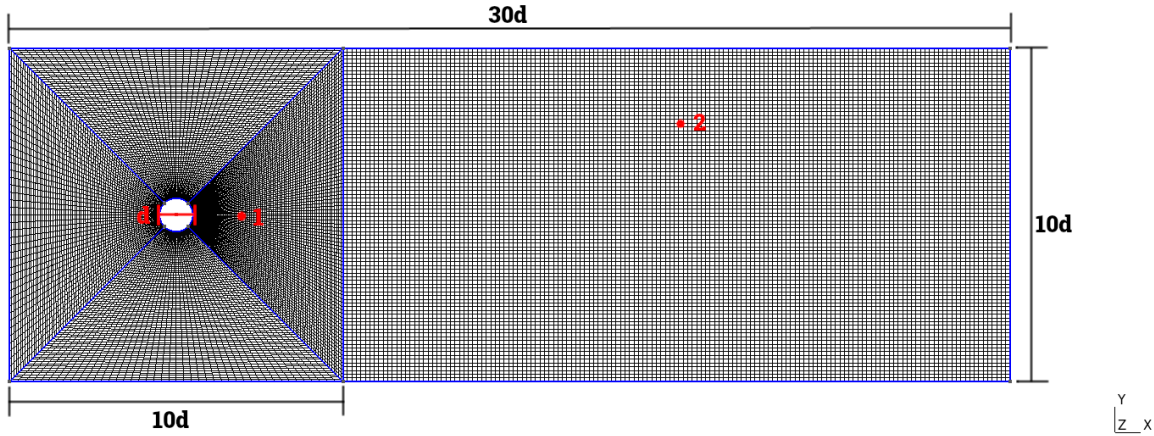


Figure 1: Computational domain with a structured 3D mesh containing 68567 cells and 44382 nodes. Locations of the two probes used are shown schematically in the figure with respective numbering. The dimensions of the computational domain are quoted as multiplies of the cylinder's diameter (d).

The boundary conditions applied to the flow field are shown in table 1. The expressions used in the table to name the boundary conditions are native to openFOAM.

Table 1: Boundary conditions applied to the computational domain.

Wall Names	Pressure	Velocity
Front and Back	empty	empty
Bottom	zeroGradient	slip
Top	zeroGradient	slip
Cylinder	zeroGradient	fixedValue (0 0 0)
Inlet	zeroGradient	fixedValue (1 0 0)
Outlet	fixedValue (uniform 0)	zeroGradient

The front and back walls have been defined as empty patches, meaning that the solver reduces the 3D problem to a 2D one. The zeroGradient and fixedValue boundary conditions are equivalent to Neumann and Dirichlet ones

respectively. The problem is reduced to an inviscid one at top and bottom walls by applying the slip condition. This removes potential and unnecessary influence of boundary layer developed at those walls on the free-stream flow that is a subject of the analysis. The inflow velocity was set to be 1 m/s as indicated by 'Inlet' velocity boundary condition in table 1. For both pressure and velocity the internal field value was set to 0.

A simulation has been carried out using three different grids to assess spatial convergence, at $Re = 25$, which is discussed in section 2.3. An overview of the meshes tested is shown in table 2. The values quoted in the table refer to 3D meshes.

Table 2: Properties of the 3D meshes that have been tested for spatial convergence at $Re = 25$.

Mesh Name	No. of elements	No. of nodes	Max skewness
M1	42287	27162	0.9374
M2	68567	44382	1.1628
M3	88877	57762	1.6724

For all the computations presented in this report, including convergence tests, the time step used was 0.0022 seconds. This allowed to maintaining Courant (CFL) number below, or equal to, 0.3 under all conditions. Simultaneously, such time step did not compromise quickness of the simulation, with the densest mesh taking about 7200 seconds to complete. The computations were carried out using a sequential computation in a Virtual-Box environment with Ubuntu 18.04.5 installed. The hardware used was Intel Core i5-8250U CPU (1.60GHz \times 8) with 8GB RAM.

2.3 Spatial and temporal convergence

Assessing temporal convergence was inconvenient as the von Kármán vortex street is an unsteady phenomenon. Instead, the time needed for the shedding to develop at moderate Reynolds number was determined. This time was then used for all computations. The trial simulations was run for $Re = 140$, using M1 mesh, and the residuals are shown in figure 2.

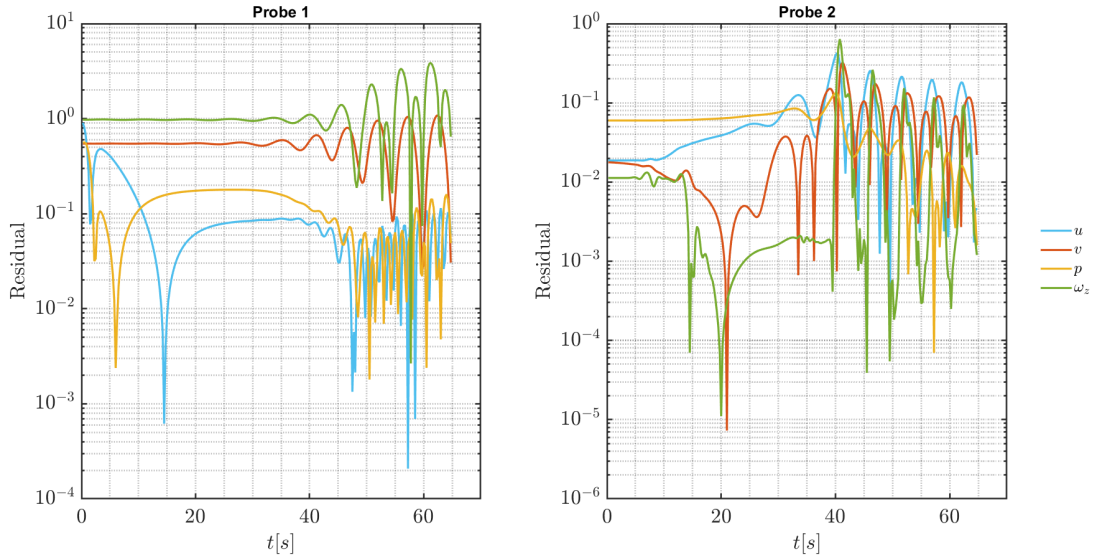


Figure 2: Residuals for probes 1 and 2 at $Re = 140$. A development of the vortex shedding can be seen as oscillations of the residuals at times larger than 40 seconds.

The figure clearly indicates that the vortex shedding develops around 40 seconds into the simulation. It can be identified by the high frequency oscillations of the residuals. Therefore, the total time of simulation being 65 seconds is deemed appropriate for the purpose of this work, as it allows for the development of the Kármán vortex street at moderate Reynolds numbers.

To determine the spatial convergence, a simulation at $Re = 25$ was run. This Reynolds number was chosen to ensure that no shedding develops and hence a steady-state can be obtained. This steady state was then used to compare performance of different meshes. Firstly, the temporal convergence has been checked for the flow at $Re = 25$ given predetermined computation time of 65 seconds. Again, the assessment of temporal convergence was done using mesh M1. The residuals are shown in figure 3.

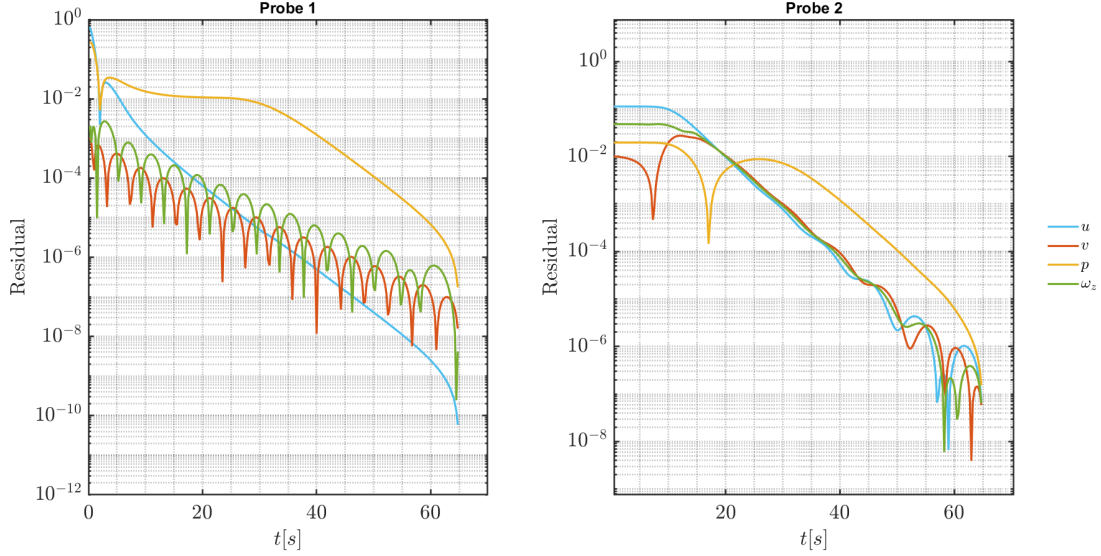


Figure 3: Residuals for probes 1 and 2 at $Re = 25$. Given computation time of 65 second, a satisfactory convergence has been achieved, with the biggest residual being pressure approaching $10E-7$ for both probes.

All the residuals decayed to a satisfactory level with the biggest one being pressure approaching $10E-7$ for both probes. Having ensured that the computation time is long enough for a temporal convergence of a laminar steady flow and to develop vortex shedding for moderate Reynolds number flow, it was possible to assess spatial convergence using the meshes tabulated in table 2. The results of the assessment are shown in table 3.

Table 3: Spatial convergence of flow behind a circular cylinder at $Re = 25$.

	Probe 1		Probe 2	
Mesh name	p [Pa]	ω_z [1/s]	p [Pa]	ω_z [1/s]
M1	-0.262430	0.0E-6	-0.020016	-0.0393016
M2	-0.29157	0.0E-6	-0.019875	-0.048518
M3	-0.291396	0.2E-6	-0.019532	-0.047556

The table above contains two flow properties that have been used as convergence indicators, i.e. pressure and vorticity. This has been done so as pressure is a very good indicator of flow behaviour in an incompressible flow. Additionally, the vorticity is computed from velocity components, thus it shows combined convergence of both. This is a more strict approach to velocity convergence as additional error is introduced due to the second-order numerical differentiation scheme used. Nevertheless, a satisfactory spatial convergence has been achieved. Based

on the convergence analysis presented above, the subsequent computations were run on M3 mesh for 65 seconds with time step of 0.0022 seconds.

3 Results

Hereinafter, the results of the simulations and post-processing are shown. The results are presented following the flow regimes breakdown proposed by Williamson (1996), which are visualised by figure 4. The flow behaves as predicted, with a clear breakdown of the regular vortex structures is shown by flow at $Re = 10E4$. Figure 4a represents laminar steady flow regime, however a trace of instabilities has been detected in the residuals analysis what matches the predictions of Roshko (1993) that the instabilities start occurring at $Re \sim 50$.

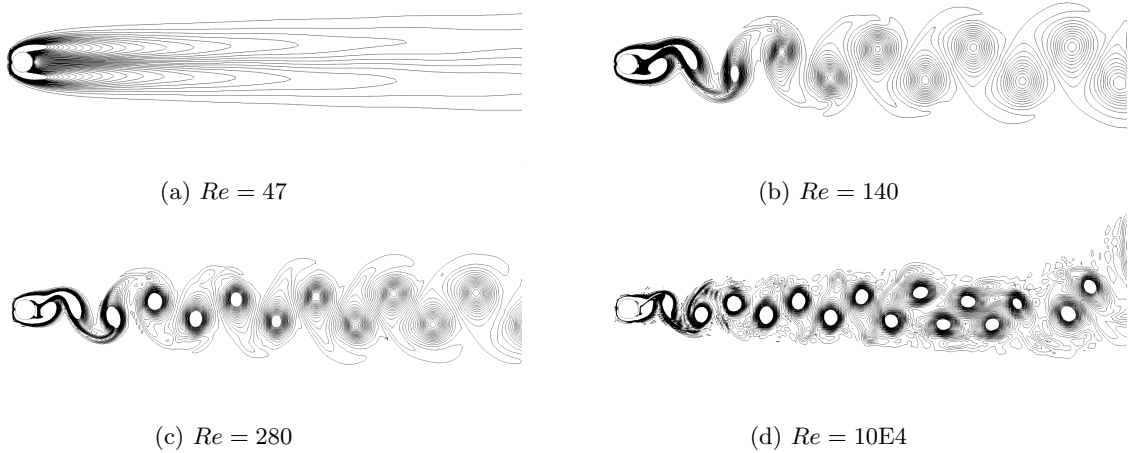


Figure 4: Visualisation of flow past a 2D circular cylinder, after 65 s, for four different Reynolds numbers, where each represents one of the flow regimes considered in this work. The figures represent vorticity, ω_z , of the flow using linearly spaced isolines in the range of $-2.0 \leq \omega_z \leq 2.0$. A clear breakdown of the regular structures emerges as the Reynolds number is increased. This is best shown by flow at $Re = 10E4$.

3.1 Laminar steady flow regime ($Re < 49$)

Two simulations have been run for the laminar steady flow regime at Reynolds numbers of 25 and 47. The aim was to determine a size of the separation bubble behind the bluff body and the drag coefficient the 2D body is experiencing.

In the separation bubble, the flow reverses what can be seen in as a negative component of the stream-wise velocity, following the convention defined by figure 1. This characteristic has been used to assess the size of the separation bubble. Firstly, the data has been extracted along a centreline of the computational domain in x-direction using Paraview functionality *plotOverLine*. In the post-processing a signum function has been applied to the obtained data set to estimate at which point the sign of the stream-wise velocity component changes and hence to determine the location of the dividing streamline. The resulting length of the separation bubble, L_{SB} , is shown in table 4. The lengths presented have been non-dimensionalised by the diameter of the cylinder.

The drag coefficient has been obtained by using a post-processing functionality of openFoam, i.e. by using *forceCoeffs* function. As the drag coefficient, C_D , tends to slightly change with time an average of this parameter has been taken. Importantly, the initial transition has been neglected in this time average to obtain more representative results to compare with literature. The drag coefficient values are also shown in table 4.

Table 4: Size of the separation bubble, L_{SB} , and the time averaged drag coefficient, $\langle C_D \rangle$, are shown for respective Reynolds numbers from the laminar steady flow regime.

Re	25	47
L_{SB}	1.2495	2.6215
$\langle C_D \rangle$	2.1922	1.7031

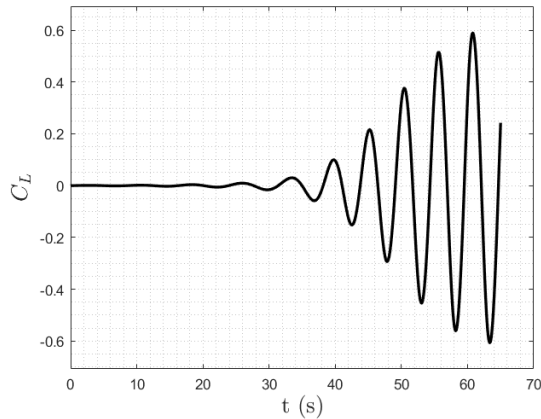
3.2 Stable laminar vortex shedding regime ($50 \leq Re \leq 150$)

In this range of Reynolds numbers, a laminar vortex shedding is expected and has been observed as depicted in 4b. The simulations have been run for three different Reynolds numbers, i.e. 80, 100 and 140. To determine the time averaged drag coefficient, exactly the same approach as previously has been applied and the results are listed in table 5. Another objective was to determine the non-dimensional Strouhal number, which is defined as

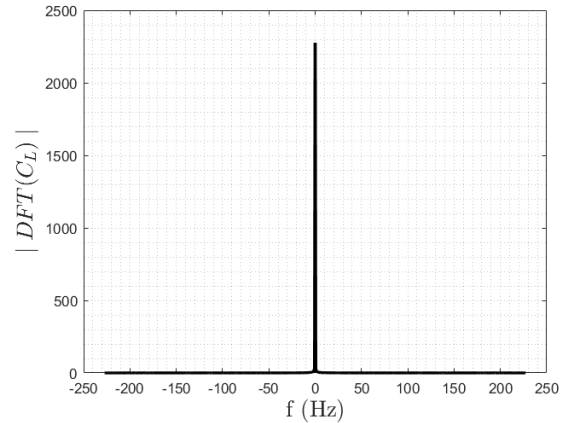
$$St = \frac{fd}{U} \quad (2)$$

where f is the frequency of vortex shedding, d is the diameter of the cylinder and U is the free-stream velocity. Due to the way this problem is constructed, with $U = 1$ m/s and $d = 1$ m, the Strouhal number is equal to the numerical value of the vortex street frequency.

The presence of vortex shedding downstream induced oscillations in force coefficients acting on the 2D cylinder. An example of such oscillation is shown in figure 5a but it also has been present in the drag coefficient. For purpose of this analysis it has been assumed that the oscillations in lift coefficient experienced by the body are a good representation of the vortex shedding period. Therefore, a discrete Fourier transform (DFT) has been applied to the lift coefficient data set. It was implemented using a fast Fourier transform (FFS) algorithm. Thanks to this methodology a leading frequency of the oscillations has been determined. The DFT was applied to the lift coefficient fluctuations as there is very little noise in the data when compared with the drag coefficient. As shown in figure 5b, this analysis gave a very distinct peak in the single-sided DFT spectrum. The leading frequency of the oscillations and the drag coefficient for each Reynolds number considered are shown in table 5



(a) Lift coefficient on the 2D cylinder as a function of time for a flow at $Re = 140$.



(b) Absolute value of a single-sided discrete Fourier transform on the data set visualised in figure 5a.

Figure 5: A fast Fourier transform algorithm has been applied to the time function of the lift coefficient, C_L , acting on the 2D cylinder at $Re = 140$. The analysis indicates a small range of dominant frequencies that are then used to establish shedding frequency, and in consequence the Strouhal number.

Table 5: Strouhal number, St , and the time averaged drag coefficient, $\langle C_D \rangle$, are shown for respective Reynolds numbers from the stable laminar vortex shedding regime.

Re	80	100	140
St	0.1693	0.1693	0.2000
$\langle C_D \rangle$	1.4508	1.4508	1.4685

3.3 Transitional regime ($150 \leq Re \leq 300$)

In this flow regime, an increased frequency of the vortex shedding can be observed, as shown in figure 4. The same figure supports [Williamson \(1996\)](#) statement about a transition to an irregular regime occurring as the shedding tends to have some small secondary structures that were not present in the lower Reynolds number regimes. Two simulations have been carried out in this regime at Reynolds numbers 160 and 280.

In order to determine the time averaged drag coefficient and the shedding frequency, the exact same methodology as previous describes, has been applied. The results are shown in table 6.

Table 6: Strouhal number, St , and the time averaged drag coefficient, $\langle C_D \rangle$, are shown for respective Reynolds numbers from the transitional regime.

Re	160	280
St	0.2154	0.2308
$\langle C_D \rangle$	1.4695	1.4956

3.4 Irregular regime ($300 \leq Re \leq 10E4$)

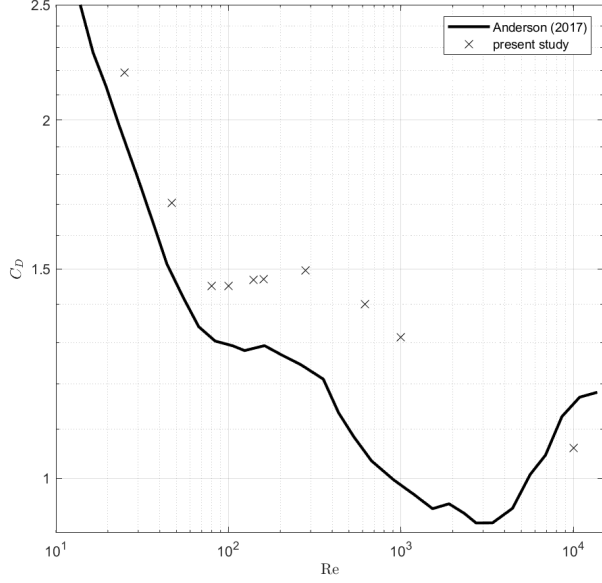
The analysis of the irregular regime is based on three simulations for which the Reynolds number was set to be 620, 1000 and 10E4. As shown in figure 4d, a clear breakdown of the regular, coherent structure is observable. The results tabulated in table 7 have been computed as described for the stable laminar vortex shedding regime.

Table 7: Strouhal number, St , and the time averaged drag coefficient, $\langle C_D \rangle$, are shown for respective Reynolds numbers from the irregular regime.

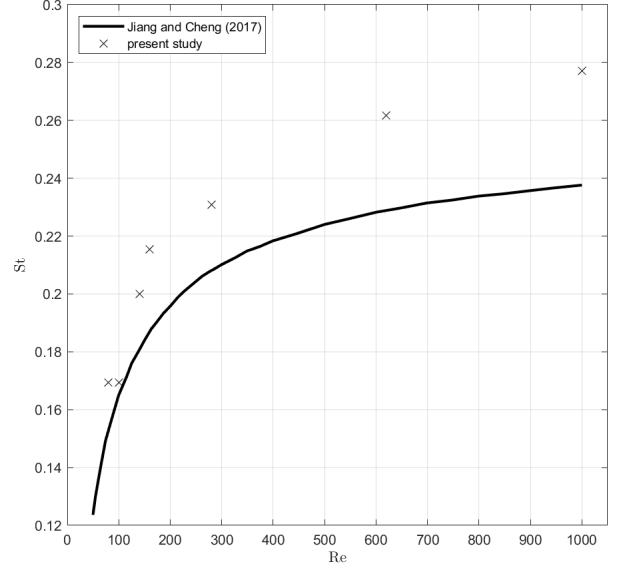
Re	620	1000	10E4
St	0.2616	0.2770	0.2923
$\langle C_D \rangle$	1.4005	1.3109	1.0610

4 Analysis and results validation

The results obtained in this numerical study are compared with existing literature to validate the methodology presented. The reference literature are works by [Anderson \(2017\)](#) and [Jiang & Cheng \(2017\)](#). The comparative study took a graphical form, and the results are visualised in figure 6. The graphs from literature have been digitalised using an online tool ([Rohatgi n.d.](#)).



(a) Comparison of the drag coefficient, C_D , dependency on the Reynolds number, Re , presented by [Anderson \(2017\)](#) and obtained from this study.



(b) Comparison of the Strouhal number, St , dependency on the Reynolds number, Re , presented by [Jiang & Cheng \(2017\)](#) and obtained from this study.

Figure 6: Comparisons of the drag coefficients and Strouhal numbers obtained from this numerical study with existing literature.

The comparison shows some discrepancies between the results obtained in this work and the literature. Nevertheless, both data sets follow the same trend. There is a few sources of errors that can explain it. Firstly, the literature results have been digitalised manually. This introduces some random error to the comparison data but such error should be small and cannot justify the offsets shown in figure 6.

Another possible cause is the insufficient spatial and temporal resolution of the simulations. Figure 6 indicates that the error increases proportionally to the Reynolds number. As the value of this non-dimensional group increases the structure of vortices become more irregular and complex, as already shown. Therefore, to properly resolve those phenomena and to accurately quantify their influence on the body, a higher spatial and temporal resolutions are needed. The need for great resolution of simulation is a know problem of the DNS. As indicated by [Zhou \(2018\)](#), a great advantage of the direct numerical simulation is undoubtedly the ability to resolve all scales without a need for any closure models. Nevertheless, even for the small computations at low Reynolds numbers flow, this approach requires great computational resources.

The resolution issue can also explain the error shown by figure 6b. This figure does not include results for Reynolds number 10E4 but the trend of an increasing error is clear. In order to obtain accurate results of shedding frequency a good temporal resolution is needed to capture the time dependency of vortices. In this study, it was aimed to maintain the maximum CFL number at about 0.3. This was deemed acceptable, but it becomes clear that in order to obtain von Kármán vortex street frequency, and hence the Strouhal number, more precisely, the maximum CFL should have much lower value. In order not to compromise the spatial resolution so much needed for DNS, CFL should be decreased by lowering the value of the time step.

Not only the high spatial and temporal requirements of DNS could cause the discrepancies between compared data. As already described, in the post-processing the drag coefficient has been time averaged excluding an initial transition. [Anderson \(2017\)](#) does not provide information on how the drag coefficient presented in his work has been calculated. Therefore, the difference in the post-processing methodology could lead to some differences in results. On the other hand, to compute the shedding frequency a DFT has been implemented on the lift coefficient. An assumption that period of the oscillations in the lift coefficient translates exactly to the period of the shedding could introduce another error to the results. Additionally, the accuracy of the DFT is highly dependent on the

sampling frequency of the signal, in this case the lift coefficient. For this study the samples have been taken in 0.0022 seconds intervals. If a higher sampling frequency was chosen, the signal could be decomposed into more frequencies and a more precise leading frequency could be determined. Insufficient sampling frequency can explain why the computed Strouhal number is the same for flow at Reynolds numbers of 80 and 100, as the FFT was unable to resolve the signal appropriately. This issue becomes more prominent as the frequency of the vortex shedding, i.e. Reynolds number, increases making the sampling frequency of 1/0.0022 Hz even more unsuitable.

In terms of the analysis of the separation bubble for the laminar steady flow regime a study published by [Franke et al. \(1990\)](#) indicates that for flow at $Re = 40$, the separation bubble behind a 2D cylinder reached a value of 2.86 cylinder diameters. This is roughly consistent with the results presented in table 4, e.g. $L_{SB} = 2.6215$ for $Re = 47$. However, this study did not cover the separation bubble to a great extent so a reliable comparative study is difficult to conduct. In order to investigate this problem further, more simulations should be run for the laminar steady flow regime.

5 Conclusion

This work presents results of direct numerical simulation of the flow behind a 2D circular cylinder. The simulations have been carried out for ten different Reynolds numbers using icoFoam which is one of the openFoam solvers. The study focused on determining the drag coefficient on the cylinder and the frequency of the vortex shedding, i.e. Strouhal number. A brief analysis of the separation bubble for low Reynolds numbers flow has been also conducted.

Thanks to the visualisation techniques, a breakdown of the flow regimes used by [Williamson \(1996\)](#) has been verified. However, some discrepancies between results obtained as part of this work and literature have been noticed. As a primary reason for these differences the high spatial and temporal resolution needed by DNS to resolve flow structures has been identified. The order of magnitude of the separation bubble's length has been confirmed with the literature but not enough data has been collected for the laminar steady flow regime to make a valid comparative study.

Should this work be continued, higher spatial and temporal resolutions should be used to validate the error analysis presented in this work and obtain more accurate results. Finally, a more comprehensive study should be conducted on the separation bubble for low Reynolds numbers flow to validate the approach presented in this work.

References

- Anderson, J. D. (2017), *Fundamentals of aerodynamics*, McGraw-Hill Education.
- Ausoni, P., Farhat, M., Ait Bouziad, Y., Kueny, J.-L. & Avellan, F. (2006), Kármán vortex shedding in the wake of a 2d hydrofoil: Measurement and numerical simulation, in ‘IAHR Int. Meeting of WG on Cavitation and Dynamic Problems in Hydraulic Machinery and Systems’, number CONF.
- Franke, R., Rodi, W. & Schönung, B. (1990), ‘Numerical calculation of laminar vortex-shedding flow past cylinders’, *Journal of Wind Engineering and Industrial Aerodynamics* **35**, 237 – 257.
URL: <http://www.sciencedirect.com/science/article/pii/0167610590902193>
- Geuzaine, C. & Remacle, J.-F. (2009), ‘Gmsh: A 3-d finite element mesh generator with built-in pre-and post-processing facilities’, *International journal for numerical methods in engineering* **79**(11), 1309–1331.
- Issa, R. I. (1986), ‘Solution of the implicitly discretised fluid flow equations by operator-splitting’, *Journal of computational physics* **62**(1), 40–65.
- Jiang, H. & Cheng, L. (2017), ‘Strouhal–reynolds number relationship for flow past a circular cylinder’, *Journal of Fluid Mechanics* **832**, 170–188.
- Larsen, A. (2000), ‘Aerodynamics of the tacoma narrows bridge-60 years later’, *Structural Engineering International* **10**(4), 243–248.
- Mittal, S., Kottaram, J. J. & Kumar, B. (2008), ‘Onset of shear layer instability in flow past a cylinder’, *Physics of Fluids* **20**(5), 054102.
- OpenCFD (2018).
URL: <https://www.openfoam.com/documentation/guides/latest/doc/guide-applications-solvers-incompressible-icoFoam.html>
- OpenCFD (2019).
URL: <https://openfoam.com/>
- Rohatgi, A. (n.d.).
URL: <https://automeris.io/WebPlotDigitizer/>
- Roshko, A. (1993), ‘Perspectives on bluff body aerodynamics’, *Journal of Wind Engineering and Industrial Aerodynamics* **49**(1-3), 79–100.
- Williamson, C. H. (1996), ‘Vortex dynamics in the cylinder wake’, *Annual review of fluid mechanics* **28**(1), 477–539.
- Zhou, L. (2018), *Theory and modeling of dispersed multiphase turbulent reacting flows*, Butterworth-Heinemann.

A openFoam files

A.1 controlDict

```
/*-----* C++ *-----*/
|=====|
| \ \ \ \ / F i e l d | OpenFOAM: The Open Source CFD Toolbox
| \ \ \ \ / O p e r a t i o n | Version: 2.4.0
| \ \ \ \ / A n d | Web: www.OpenFOAM.org
| \ \ \ \ / M a n i p u l a t i o n |
/*-----*/
FoamFile
{
    version      2.0;
    format       ascii;
    class        dictionary;
    location     "system";
    object       controlDict;
}
// * * * * *

application      icoFoam;      // opt icoFoam simpleFoam pisoFoam pimpleFoam

startFrom         latestTime;   // opt: firstTime startTime latestTime

startTime         0;           // opt: 0

stopAt            endTime;     // opt: endTime writeNow noWriteNow nextWrite

endTime           65;

deltaT            0.0022;

writeControl       runtime;     // opt: timeStep runtime adjustableRunTime cpuTime clockTime

writeInterval      0.25;

purgeWrite         0;

writeFormat        ascii;

writePrecision     12;

writeCompression   off;

timeFormat         general;

timePrecision      12;

runtimeModifiable no;
```

```

adjustTimeStep  yes;

maxCo           0.3;

functions
{
    #includeFunc vorticity
    #includeFunc probesPrim
    #includeFunc probesVort

    forces
    {

        #includeEtc "caseDicts/postProcessing/forces/forcesIncompressible.cfg"

        rhoInf      1.0;      // Fluid density
        patches      (cylinderWalls);

        CofR         (0 0 0);
        pitchAxis     (0 1 0);

        log true;
        utputControl runTime;
        outputInterval 0.25;
    }

    forceCoeffs
    {
        // rhoInf - reference density
        // CofR - Centre of rotation
        // dragDir - Direction of drag coefficient
        // liftDir - Direction of lift coefficient
        // pitchAxis - Pitching moment axis
        // magUinf - free stream velocity magnitude
        // lRef - reference length
        // Aref - reference area

        type forceCoeffs;
        functionObjectLibs ("libforces.so");
        patches (cylinderWalls);
        pName p;
        Uname U;
        rho rhoInf;
        rhoInf 1.0;

        //Dump to file
        log true;
        CofR (0.0 0 0);
        liftDir (0 1 0);
        dragDir (1 0 0);
        pitchAxis (0 0 1);
    }
}

```

```

        magUInf 1.0;
        lRef 1.0; // reference lenght
        Aref 1.0; // reference area 1 for 2d

        utputControl runTime;
        outputInterval 0.25;
    }

}
// ***** //

```

A.2 probesPrim

```
probesPrim
{
  functionObjectLibs ( "libsampling.so");
  type probes;
  name probes;
  writeControl runTime;
  writeInterval 0.25;

  fields
  (
    U
    p
  );

  probeLocations
  (
    (1.0 0.0 0) // behind the cylinder
    (10 2.5 0) // in the wake
  );

}
```


A.3 probesVort

```
probesVort
{
  functionObjectLibs ( "libsampling.so");
  type probes;
  name probes;
  writeControl runTime;
  writeInterval 0.25;
  fields (
    vorticity
  );

  probeLocations
  (
    (1.0 0.0 0) // behind the cylinder
    (10 2.5 0) // in the wake

  );

}
```

A.4 transportProperties

```
/*-----* C++ *-----*\
|  ==  | F i e l d | OpenFOAM: The Open Source CFD Toolbox
|  \ \  | O p e r a t i o n | Version: 2.4.0
|  \ \  | A n d | Web: www.OpenFOAM.org
|  \ \  | M a n i p u l a t i o n |
\*-----*/
FoamFile
{
    version      2.0;
    format       ascii;
    class        dictionary;
    location     "constant";
    object       transportProperties;
}
// * * * * *

transportModel  Newtonian;

nu              nu [ 0 2 -1 0 0 0 0 ] .00357142857; /* Re = 280

// *****
```

A.5 ./0/p

```

/*-----* C++ *-----*/
|=====|
|  \ \  /  F i e l d      | OpenFOAM: The Open Source CFD Toolbox
|  \ \  /  O p e r a t i o n      | Version: 2.4.0
|  \ \  /  A n d      | Web: www.OpenFOAM.org
|  \ \  /  M a n i p u l a t i o n      |
|=====|
/*-----*/
FoamFile
{
    version      2.0;
    format       ascii;
    class        volScalarField;
    location     "0";
    object       p;
}
// * * * * *

dimensions      [0 2 -2 0 0 0 0];

internalField    uniform 0;

boundaryField
{
    frontAndBack
    {
        type      empty;
    }
    bottom
    {
        type      zeroGradient;
    }
    cylinderWalls
    {
        type      zeroGradient;
    }
    top
    {
        type      zeroGradient;
    }
    inlet
    {
        type      zeroGradient;
    }
    outlet
    {
        type      fixedValue;
        value      uniform 0;
    }
}

```

// ***** //

A.6 ./0/U

```

/*-----* C++ *-----*/
|=====|
|  \ \  /  F i e l d      | OpenFOAM: The Open Source CFD Toolbox
|  \ \  /  O p e r a t i o n | Version: 2.4.0
|  \ \  /  A n d             | Web: www.OpenFOAM.org
|  \ \  /  M a n i p u l a t i o n |
|=====|
/*-----*/
FoamFile
{
    version      2.0;
    format       ascii;
    class        volVectorField;
    location     "0";
    object       U;
}
// * * * * *

dimensions      [0 1 -1 0 0 0 0];

internalField    uniform (0 0 0);

boundaryField
{
    frontAndBack
    {
        type            empty;
    }
    bottom
    {
        type            slip;
    }
    cylinderWalls
    {
        type            fixedValue;
        value            uniform (0 0 0);
    }
    top
    {
        type            slip;
    }
    inlet
    {
        type            fixedValue;
        value            uniform (1 0 0);
    }
    outlet
    {
        type            zeroGradient;
    }
}

```

// ***** //

B Gmsh geometry

```
// Gmsh project created on Wed Sep 30 21:41:07 2015
// Author: Martin Einarsve
// Modified by Vassilis Theofilis on Apr 18, 2017
// Modified by Kamil Dylewicz on Dec 17, 2020

Nx1 = 70; Rx1 = 1.00;
Nx2 = 150; Rx2 = 1.00;
Ny1 = 90; Ry1 = 1.00;
Ni = 70; Ri = 1.00;
Nc = 45; Rc = 1.00;

Point(1) = {-5, -5, 0, 1.0};
Point(2) = { 5, -5, 0, 1.0};
Point(3) = {25, -5, 0, 1.0};

Point(4) = {-0.353553, -0.353553, 0, 1.0};
Point(5) = { 0.353553, -0.353553, 0, 1.0};
Point(6) = {-0.353553, 0.353553, 0, 1.0};
Point(7) = { 0.353553, 0.353553, 0, 1.0};

Point(8) = {-5, 5, 0, 1.0};
Point(9) = { 5, 5, 0, 1.0};
Point(10) = {25, 5, 0, 1.0};
Point(11) = { 0, 0, 0, 1.0};

Line(1) = {1, 2}; Transfinite Line {1} = Nc Using Progression Rc;
Line(2) = {2, 3}; Transfinite Line {2} = Nx2 Using Progression Rx2;
Line(3) = {8, 9}; Transfinite Line {3} = Nc Using Progression Rc;
Line(4) = {9, 10}; Transfinite Line {4} = Nx2 Using Progression Rx2;
Line(5) = {1, 8}; Transfinite Line {5} = Nc Using Bump Rc;
Line(6) = {2, 9}; Transfinite Line {6} = Ny1 Using Bump Ry1;
Line(7) = {3, 10}; Transfinite Line {7} = Ny1 Using Bump Ry1;
Line(8) = {1, 4}; Transfinite Line {8} = Ni Using Progression Ri;
Line(9) = {2, 5}; Transfinite Line {9} = Ni Using Progression Ri;
Line(10) = {9, 7}; Transfinite Line {10} = Ni Using Progression Ri;
Line(11) = {8, 6}; Transfinite Line {11} = Ni Using Progression Ri;

Circle(12) = {4, 11, 5}; Transfinite Line {12} = Nc Using Progression Rc;
Circle(13) = {5, 11, 7}; Transfinite Line {13} = Ny1 Using Progression Ry1;
Circle(14) = {7, 11, 6}; Transfinite Line {14} = Nc Using Progression Rc;
Circle(15) = {6, 11, 4}; Transfinite Line {15} = Nc Using Progression Rc;

Line Loop(16) = {1, 9, -12, -8};
Plane Surface(17) = {16};
Line Loop(18) = {9, 13, -10, -6};
Plane Surface(19) = {18};
Line Loop(20) = {10, 14, -11, 3};
Plane Surface(21) = {20};
```

```

Line Loop(22) = {11, 15, -8, 5};
Plane Surface(23) = {22};
Line Loop(24) = {2, 7, -4, -6};
Plane Surface(25) = {24};
Transfinite Surface {17};
Transfinite Surface {19};
Transfinite Surface {21};
Transfinite Surface {23};
Transfinite Surface {25};

Recombine Surface {17};
Recombine Surface {19};
Recombine Surface {21};
Recombine Surface {23};
Recombine Surface {25};

Extrude {0, 0, 1} {
  Surface{17, 19, 21, 23, 25};
  Layers{1};
  Recombine;
}

Physical Surface("inlet") = {112}; // inlet
Physical Surface("outlet") = {126}; //outlet
Physical Surface("top") = {90, 130}; // top
Physical Surface("bottom") = {34, 122}; // bottom
Physical Surface("frontAndBack") = {47, 69, 91, 113, 135, 17, 19, 21, 23, 25};
// frontAndBack
Physical Surface("cylinderWalls") = {104, 42, 60, 82}; //cylinderWalls
Physical Volume("internal") = {1, 2, 3, 4, 5}; // internal

```